

Research Article

Simulation of the Damage Process in Quasi-Brittle Materials by a Modified Finite Element Method Using the Consistent Embedded Discontinuity Formulation

J. Retama ¹ and A. G. Ayala ²

¹Department of Civil Engineering, FES Aragón, National Autonomous University of Mexico, Mexico City, Mexico

²Department of Structural Engineering, Institute of Engineering, National Autonomous University of Mexico, Mexico City, Mexico

Correspondence should be addressed to J. Retama; jretamav@comunidad.unam.mx

Received 2 October 2019; Revised 21 October 2020; Accepted 2 November 2020; Published 30 November 2020

Academic Editor: Giovanni Garcea

Copyright © 2020 J. Retama and A. G. Ayala. This is an open access article distributed under the Creative Commons Attribution License, which permits unrestricted use, distribution, and reproduction in any medium, provided the original work is properly cited.

This paper investigates the variational finite element formulation and its numerical implementation of the damage evolution in solids, using a new discrete embedded discontinuity approach. For this purpose, the kinematically optimal symmetric (KOS) formulation, which guarantees kinematics, is consistently derived. In this formulation, rigid body motion of the parts in which the element is divided is obtained. To guarantee equilibrium at the discontinuity surfaces, the length of the discontinuity is introduced in the numerical implementation at elemental level. To illustrate and validate this approach, two examples, involving mode-I failure, are presented. Numerical results are compared with those reported from experimental tests. The presented discontinuity formulation shows a robust finite element method to simulate the damage evolution processes in quasi-brittle materials, without modifying the mesh topology when cohesive cracks propagate.

1. Introduction

The numerical simulation of the development and growth of cohesive cracks in quasi-brittle materials has posed a scientific challenge to structural engineering for decades. For this, two main paths can be distinguished: the modelling of the damage process in a smeared sense [1–3], within a continuum theory, and the modelling of cohesive cracks in a discrete form [4–6].

Within the FEM context, two different types of models may be distinguished: one in which the inelastic deformation of the fracture process zone is smeared over a band of a certain width and the other in which the entire fracture process is lumped into a crack line whose behaviour is characterized by a stress-displacement law, known as cohesive zone models [1, 6–8].

In the discrete modelling of fractures, the cohesive forces across a crack are modelled as a progressive degradation of

the mechanical properties of the material (Figure 1), and a stress-displacement relationship is used [9].

For the case of brittle material and considering a Rankine criterion failure, the crack begins to grow once the principal stress σ_I reaches the tensile strength σ_{t0} . The work energy G_F needed to create a fully developed crack of unit area is as follows [1, 10]:

$$G_F = \int_0^u \sigma d\mu, \quad (1)$$

where σ and μ are the stress and displacement, respectively, defined on the cohesive crack (Figure 1).

Recently, a different approach in which the crack crosses the element (Figure 2) has been developed. This approach emerged as a mean to deal with general strain localization phenomena, of which the cohesive crack is a case (see [5, 11–17]).

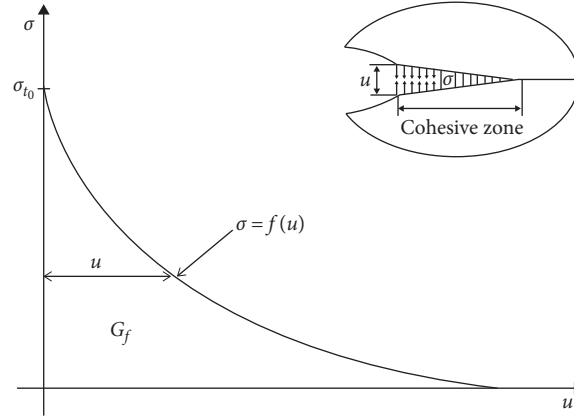


FIGURE 1: Fictitious crack model.

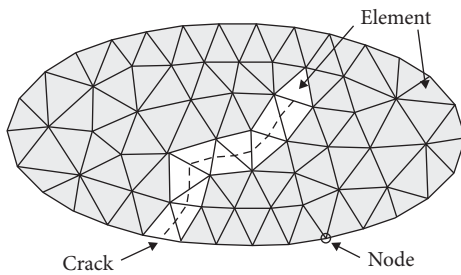


FIGURE 2: Embedded discontinuity models.

All embedded discontinuity approaches have a common basic underlying; the process zone is incorporated into the variational formulation of the finite element model, by an enhancement of the relevant fields interpolation, which bears the required discontinuity only where it appears without affecting the main fields [4, 5, 18].

Depending on the use of the constitutive model and the kinematics of displacements and strains, three embedded discontinuity formulations are identified: weak discontinuity, strong discontinuity, and discrete discontinuity [19].

The weak discontinuity model considers that the displacement field is continuous and the strain field is discontinuous. In this model, the damage process zone is located into a bandwidth different from zero (Figure 3(a)). When the bandwidth tends to zero, the strong discontinuity model is recovered, making the displacements field discontinuous, and the strains are unbounded across the discontinuity (Figure 3(b)).

The third model is the discrete discontinuity approach in which, unlike the strong discontinuity, the former considers two constitutive laws, one strain-stress for the bulk and other traction-jump for the cohesive crack zone [5, 18, 19] (Figure 3(c)).

In this paper, the discrete embedded discontinuity is used to simulate damage process in quasi-brittle materials, like concrete and rocks [5, 17].

2. Embedded Discontinuities

The need of accurately modelling phenomena that present strong discontinuity in the fields of the state variables arises

in many fields of the mechanics of materials and structures. The strong discontinuity approach (SDA) has proven effective in treating many problems in the mechanics of solids which considers discontinuous fields. Its basic idea is to introduce an enhancement in the interpolation of the relevant fields, which bears the required discontinuity only where it appears so that the model of the main field is not affected by the enhancement (Figure 2).

The idea is shared between methods that enrich the nodal variables (XFEM) and methods that use elements with embedded discontinuities (EED). The latter methods appear very convenient since the additional degrees of freedom enter the equations only locally and can be treated in the same way as inelastic strains [4, 5, 11–16, 20–22].

There exist many formulations for EED [13, 19] that differ mainly in the numerical implementation of the method since the kinematic assumptions are basically the same as those originally proposed by Simo [23]. Furthermore, it appears that most of the formulations have been developed within the framework of constant stress elements or at least for elements with constant enhanced strains (see [24, 25]).

Within the framework of the embedded discontinuity formulation, three different approaches may be identified attending to the constitutive models employed and the used kinematics of displacement and strain fields [19]. In this paper, the kinematically optimal symmetric (KOS) embedded discontinuity formulation is addressed, and attention is devoted to the kinematics of the enhancement displacement field. As explained in the paper by Jirásek [19], using the standard interpolation of the enhanced displacement field, a Ritz–Galerkin procedure produces a symmetric formulation but violates the equilibrium condition on the interface.

3. Kinematics of the Discontinuity

To establish the kinematics of the discontinuity interface, consider a body with domain Ω and boundary Γ (Figure 4), where essential boundary conditions $\bar{\mathbf{u}}$ are imposed on Γ_u and natural boundary conditions $\bar{\mathbf{t}}$ are applied on Γ_t , such that $\Gamma = \Gamma_u \cup \Gamma_t$ and $\emptyset = \Gamma_u \cap \Gamma_t$. Additionally, the body is

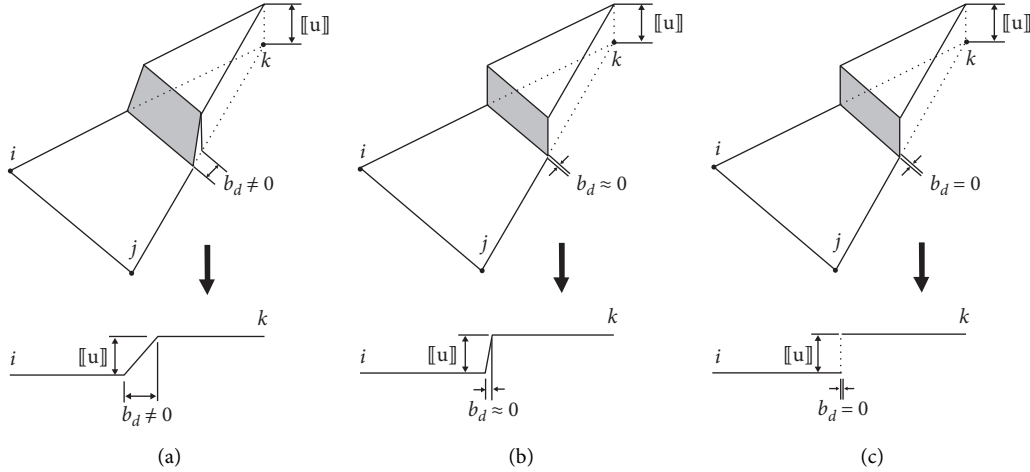
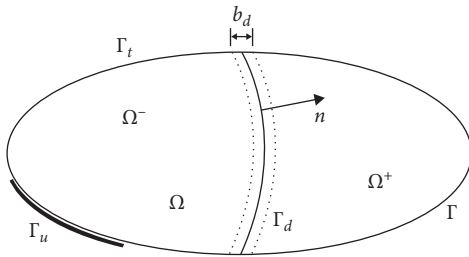


FIGURE 3: FEM mesh of a solid with an internal crack.


 FIGURE 4: Continuum solid crossed by a discontinuity Γ_d .

crossed by a discontinuity Γ_d , dividing the body domain Ω in two subdomains Ω^+ and Ω^- . On the discontinuity boundary, the normal vector \mathbf{n} is defined pointed towards Ω^+ .

The strong discontinuity approach, addressed in this paper, can be regarded as a limit case of the weak discontinuity when the width of the localizations zone b_d tends to zero, collapsing into a localized surface Γ_d . For this, when the strength of the material is reached, the deformation due to microcracking or other inelastic phenomena suddenly localizes into the discontinuity surface.

3.1. Displacement Jump. The displacement field \mathbf{u} for the body crossed by a discontinuity, shown in Figure 4, is decomposed into a continuous and discontinuous part [16, 22, 26].

$$\mathbf{u}(\mathbf{x}) = \hat{\mathbf{u}}(\mathbf{x}) + \mathcal{H}_{\Gamma_d}(\mathbf{x})[[\mathbf{u}]](\mathbf{x}), \quad (2)$$

where $\hat{\mathbf{u}}$ and $[[\mathbf{u}]]$ are smooth and continuous functions defined on Ω , with Cartesian coordinates \mathbf{x} , and \mathcal{H}_{Γ_d} is the Heaviside function centred at the discontinuity surface defined as

$$\mathcal{H}_{\Gamma_d}(\mathbf{x}) = \begin{cases} \alpha_d, & \forall \mathbf{x} \in \Omega^+, \\ 1 - \alpha_d, & \forall \mathbf{x} \in \Omega^-. \end{cases} \quad (3)$$

The parameter α_d , $0 \leq \alpha_d \leq 1$, defines the way as the jump is transmitted: for $\alpha_d = 0$, the jump is transferred to Ω^+ , while for $\alpha_d = 1$ it is transferred to Ω^- .

The corresponding infinitesimal strain field can be derived by taking the symmetric gradient of equation (2), and this is given as

$$\begin{aligned} \boldsymbol{\varepsilon} &= \nabla^s \hat{\mathbf{u}} + \mathcal{H}_{\Gamma_d}(\nabla^s [[\mathbf{u}]]) + (\nabla \mathcal{H}_{\Gamma_d} \otimes [[\mathbf{u}]])^s \\ &= \hat{\boldsymbol{\varepsilon}} + \delta_{\Gamma_d} ([[\mathbf{u}]])^s, \end{aligned} \quad (4)$$

where δ_{Γ_d} is the Dirac-delta distribution centred at the discontinuity Γ_d , satisfying

$$\int_{\Omega} \delta_{\Gamma_d} \phi \, d\Omega = \int_{\Gamma_d} \phi \, d\Gamma. \quad (5)$$

The strain field, given by equation (4), is decomposed into a bounded part $\hat{\boldsymbol{\varepsilon}}$ plus an unbounded part, irregular part, given by $\delta_{\Gamma_d} ([[\mathbf{u}]])^s$. The unbounded strains may be considered in two different ways: (1) regularizing the Dirac-delta by means of a bandwidth parameter close to zero $b_d \approx 0$ (see [15, 22, 27]) or (2) with nonregularization which implies taking advantage of Dirac-delta function defined in equation (5) (see [26, 28, 29]).

3.2. Kinematic Interpolation. The displacement and strain fields will be constructed only from kinematic considerations like in [12, 14]. For this, consider a one-dimensional finite element crossed by the discontinuity Γ_d , as it is shown in Figure 5.

It is assumed that Ω^+ undergoes a rigid body incremental displacement $\tilde{\mathbf{u}}$ with respect to Ω^- . To obtain the same incremental displacement derivatives on both subdomains, the interpolations represented in Figure 5 by lines 1 and 2 may be adopted for Ω^- and Ω^+ , respectively. Their mathematical expressions are as follows:

$$u_1 = \mathbf{N} \left[\mathbf{u} - \begin{pmatrix} 0 \\ 1 \end{pmatrix} \tilde{\mathbf{u}} \right] \quad (6)$$

for Ω^- and

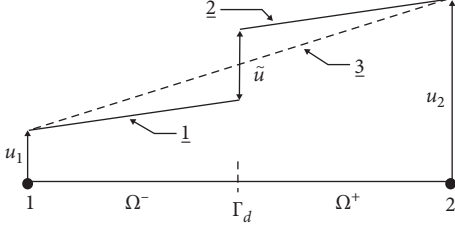


FIGURE 5: One-dimensional finite element with a discontinuity.

$$u_2 = \mathbf{N} \left[\mathbf{u} - \begin{pmatrix} 0 \\ 1 \end{pmatrix} \tilde{u} \right] + \tilde{u} \quad (7)$$

for Ω^+ . The purpose of matrix $\mathcal{H}_{\Gamma_d} = (0 \ 1)^T$, stated in equations (6) and (7), is derived from Figure 5. For every point in Ω^- or Ω^+ , the strain field is defined by

$$\boldsymbol{\varepsilon} = \nabla^s \mathbf{u} = \mathbf{B} \left[\mathbf{u} - \begin{pmatrix} 0 \\ 1 \end{pmatrix} \tilde{u} \right] = \mathbf{B}(\mathbf{u} - \mathcal{H}_{\Gamma_d} \tilde{u}), \quad (8)$$

where \mathbf{B} is the usual compatibility matrix, relating displacements and strains [30–32], and the matrix \mathcal{H}_{Γ_d} is defined in equation (3).

For a two-dimensional case, these concepts can be properly generalized by introducing the vector $\llbracket \mathbf{u} \rrbracket$ containing the components of jump displacements associated with the discontinuity Γ_d :

$$\llbracket \mathbf{u} \rrbracket = \begin{bmatrix} \tilde{u} \\ \tilde{v} \end{bmatrix}. \quad (9)$$

For this case, the matrix \mathcal{H}_{Γ_d} is derived by a straightforward generalization of its counterpart in equations (6) and (7). Its form for a two-dimensional case is written as

$$\mathcal{H}_{\Gamma_d} = \begin{bmatrix} \mathcal{H}_{\Gamma_d}^1 \\ \vdots \\ \mathcal{H}_{\Gamma_d}^n \end{bmatrix}, \quad (10)$$

where n is the number of nodes in the finite element, and each of the submatrices $\mathcal{H}_{\Gamma_d}^i$ depends on the position of node i relative to the discontinuity given as

$$\mathcal{H}_{\Gamma_d}^i = \begin{cases} \alpha_d \mathbf{I}, & \forall \mathbf{x} \in \Omega^+, \\ (1 - \alpha_d) \mathbf{I}, & \forall \mathbf{x} \in \Omega^-, \end{cases} \quad (11)$$

where \mathbf{I} is an identity matrix with dimensions $(n_{st} \times n_{st})$ and n_{st} is the space dimension of the problem.

With respect to the displacement field, this is derived from equations (6) and (7) for whole domain Ω as

$$\mathbf{u} = \mathbf{N} \hat{\mathbf{u}} + (\mathcal{H}_{\Gamma_d} - \mathbf{N} \mathcal{H}_{\Gamma_d}) \llbracket \mathbf{u} \rrbracket, \quad (12)$$

and taking \mathbf{N}_c as

$$\mathbf{N}_c = \mathcal{H}_{\Gamma_d} - \mathbf{N}_u \mathcal{H}_{\Gamma_d}, \quad (13)$$

equation (12) is written in the following final form:

$$\mathbf{u} = \mathbf{N} \hat{\mathbf{u}} + \mathbf{N}_c \llbracket \mathbf{u} \rrbracket. \quad (14)$$

The strain kinematic is derived, in a finite element framework, by means of the displacement field given by equation (14) as

$$\boldsymbol{\varepsilon} = \mathbf{B} \hat{\mathbf{u}} + \mathbf{B}_c \llbracket \mathbf{u} \rrbracket, \quad (15)$$

where the matrix \mathbf{B}_c is derived by applying the strain-displacement operator to equation (13), and this is given as

$$\mathbf{B}_c = \nabla^s \mathbf{N}_c. \quad (16)$$

Equations (14) and (15) define the displacement and strain fields, respectively, corresponding to the discrete approach of the present embedded discontinuity formulation [14, 33].

For the case of the constant strain triangle finite element and considering a uniform deformation along the internal interface (Figure 6), equation (16) is rewritten in the form

$$\mathbf{B}_c = -\nabla^s \varphi(\mathbf{x}), \quad (17)$$

where $\varphi(\mathbf{x})$ contains the shape functions corresponding to nodes in Ω^+ (see [27, 29, 33]) defined as

$$\varphi(\mathbf{x}) = \sum_{i=1}^{n^+} N_i^+, \quad (18)$$

where n^+ denotes the number of nodes belonging to the subdomain Ω^+ .

4. Discrete Damage Model

For modelling the evolution of material damage where mode-I type failure is dominant, a cohesive crack model is used (see [1, 6, 7, 34–36]). Microcracking and plastic flow around a macroscopic crack tip are modelled as equivalent tractions forces on crack faces (Figure 7).

A discontinuity is introduced when the maximum principal stress σ_I exceeds the tensile strength of the material. This mode-I criterion is commonly used for quasi-brittle materials (see [16, 26, 29]). Since the material around the discontinuity remains elastic, two constitutive models are used: one linear elastic for the bulk and other discrete damage for the discontinuity surface.

For this discrete damage model, the Helmholtz free energy density $\psi(\llbracket \mathbf{u} \rrbracket, \omega(\kappa))$, representing the free energy per unit area [16, 26] is expressed as

$$\psi(\llbracket \mathbf{u} \rrbracket, \omega(\kappa)) = [1 - \omega(\kappa)] \psi_0(\llbracket \mathbf{u} \rrbracket), \quad (19)$$

with $\llbracket \mathbf{u} \rrbracket$ already defined in Section 3.2, κ is an internal scalar variable which can be considered as an equivalent jump ($\kappa = \llbracket u \rrbracket_{eq}$), and ψ_0 is the linear elastic free energy given by

$$\psi_0(\llbracket \mathbf{u} \rrbracket) = \frac{1}{2} \llbracket \mathbf{u} \rrbracket^T \mathbf{T}^{el} \llbracket \mathbf{u} \rrbracket, \quad (20)$$

where \mathbf{T}^{el} is the elastic constitutive tensor. Equation (20) is valid for a discontinuity with a linear elastic behaviour. For adiabatic problems, the Helmholtz free energy, given by equation (19), must satisfy the Clausius–Duhem inequality (see [2, 37, 38]):

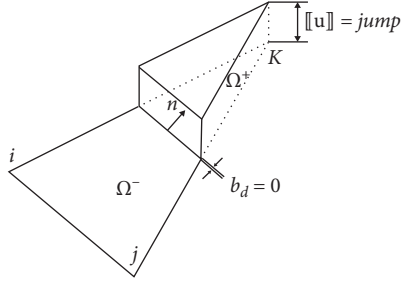


FIGURE 6: Constant strain triangle with a displacement jump.

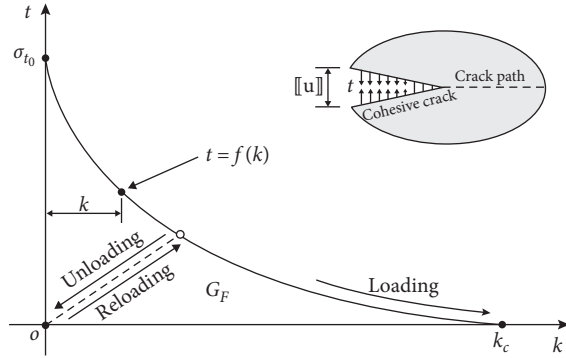


FIGURE 7: Softening curve for a cohesive crack model.

$$\mathcal{D} = \mathbf{t}^T [\dot{\mathbf{u}}] - \dot{\psi} \geq 0. \quad (21)$$

Equation (21) is a dissipative potential with \mathcal{D} being the rate of dissipation energy and \mathbf{t} the tractions vector across the discontinuity. Expanding the dissipative potential equation (21) and grouping similar terms,

$$\mathcal{D} = \left(\mathbf{t} - \frac{\partial \psi}{\partial \mathbf{u}} \right)^T [\dot{\mathbf{u}}] + \psi_0 \dot{\omega} \geq 0. \quad (22)$$

Use of standard thermodynamics arguments, in equation (21), leads to the following:

(1) Constitutive equation

$$\mathbf{t} = \frac{\partial \psi}{\partial [\mathbf{u}]} = (1 - \omega) \mathbf{T}^{\text{el}} [[\mathbf{u}]]. \quad (23)$$

(2) In addition, the dissipation equation is reduced to

$$\mathcal{D} = \psi_0 \dot{\omega} \geq 0. \quad (24)$$

Since the elastic free energy, defined per unit area, is positive, it may be seen from equation (24) that the rate of change of the damage parameter ω cannot be negative, i.e., monotonic damage process.

4.1. Tangent Constitutive Tensor. Transformation of equation (23) into its incremental form, by its differentiation with

respect to time, leads to the tangent constitutive tensor expressed as follows:

$$\dot{\mathbf{t}} = (1 - \omega) \mathbf{T}^{\text{el}} [[\dot{\mathbf{u}}]] - \dot{\omega} \mathbf{T}^{\text{el}} = (1 - \omega) \mathbf{T}^{\text{el}} [[\dot{\mathbf{u}}]] - \dot{\omega} \mathbf{t}^{\text{el}}, \quad (25)$$

where \mathbf{t}^{el} is the elastic traction vector and

$$\dot{\omega} = \frac{d\omega}{d\kappa} \frac{\partial \kappa}{\partial [[\mathbf{u}]]} [[\dot{\mathbf{u}}]] = \frac{d\omega}{d\kappa} \left[\frac{\partial \kappa}{\partial [[u]]_n} [[\dot{u}]_n] + \frac{\partial \kappa}{\partial [[u]]_s} [[\dot{u}]_s] \right]. \quad (26)$$

Substitution of equation (26) into equation (25) leads to

$$\dot{\mathbf{t}} = \left[(1 - \omega) \mathbf{T}^{\text{el}} - \frac{d\omega}{d\kappa} \mathbf{t}^{\text{el}} \otimes \frac{\partial \kappa}{\partial [[\mathbf{u}]]} \right] \cdot [[\dot{\mathbf{u}}]]. \quad (27)$$

If unloading takes place, the rate of damage is zero, i.e., $\dot{\omega} = 0$, and equation (27) reduces to

$$\dot{\mathbf{t}} = (1 - \omega) \mathbf{T}^{\text{el}} \dot{\mathbf{u}}. \quad (28)$$

4.2. Yield Function. Development of a discrete damage model requires the definition of a yield function for describing the loading state at the discontinuity surface (loading or unloading/reloading). The functions which describe this process is defined as

$$f = \langle [[u]]_{\text{eq}} \rangle - \kappa \leq 0, \quad (29)$$

where $[[u]]_{\text{eq}}$ is an equivalent jump obtained from the displacement jump vector $[[\mathbf{u}]]$. The symbols $\langle \cdot \rangle$ are the McAuley brackets denoting that only the positive part of $[[u]]_{\text{eq}}$ is considered. The internal scalar variable κ is a history parameter equal to the largest value of $\langle [[u]]_{\text{eq}} \rangle$, and this is given as

$$\kappa = \kappa([[\mathbf{u}]]) = \max \langle [[u]]_{\text{eq}} \rangle. \quad (30)$$

4.3. Loading/Unloading Conditions. If $f < 0$, the deformation process is reversible and the dissipation rate must be zero, which implies that $\dot{\omega} = 0$. If $f = 0$, the damage can grow in a way that, in a subsequent state, f remains zero ($\dot{\omega} > 0 \Rightarrow f = 0$). Both cases can be conveniently expressed by the usual Kuhn–Tucker conditions [38],

$$\begin{aligned} \dot{\omega} &\geq 0, \\ f &\leq 0, \\ \dot{\omega} f &= 0, \end{aligned} \quad (31)$$

together with the consistency condition

$$\dot{\omega} \dot{f} = 0. \quad (32)$$

5. Variational and Numerical Formulation

5.1. Variational Formulation. For this, consider a solid divided by a discontinuity Γ_d in Ω^- and Ω^+ subdomains, as shown in Figure 8, where the normal vector \mathbf{n} is placed on the discontinuity surface, and the relative displacement

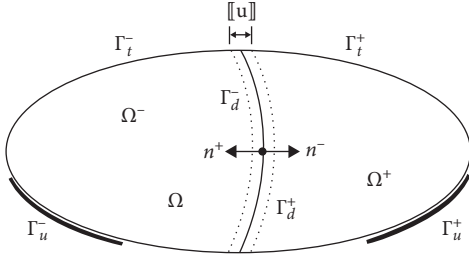


FIGURE 8: Continuum solid divided by the discontinuity Γ_d .

between both subdomains is defined by the jump $[[\mathbf{u}]]$ in the displacement field \mathbf{u} .

The energy functional for this solid is given by

$$\Pi(\mathbf{u}, [[\mathbf{u}]]) = \int_{\Omega} [\Psi(\boldsymbol{\varepsilon}) - \mathbf{u}^T \mathbf{b}_v] d\Omega - \int_{\Gamma_t} \mathbf{u}^T \bar{\mathbf{t}} d\Gamma + \int_{\Gamma_d} \psi([[\mathbf{u}]]) d\Gamma, \quad (33)$$

where $\psi([[\mathbf{u}]])$ is an additional term which considers the elastic free energy density defined on the discontinuity derived from the field $[[\mathbf{u}]]$. For a discontinuity with an elastic behaviour, this function is given by

$$\psi([[\mathbf{u}]]) = \int_0^{[[u]]} \mathbf{t}^T d[[\mathbf{u}]], \quad (34)$$

and with \mathbf{t} being the tractions vector derived from a cohesive traction-jump constitutive relation, $\mathbf{t} = \mathbf{T}[[\mathbf{u}]]$. Furthermore, for a discontinuity with a linear elastic behaviour, $\psi([[\mathbf{u}]])$ is written as

$$\psi([[\mathbf{u}]]) = \frac{1}{2} [[\mathbf{u}]]^T \mathbf{T} [[\mathbf{u}]]. \quad (35)$$

Applying the first variation to the energy functional defined in equation (33), the next Euler–Lagrange equations are recovered:

$$\nabla^T \boldsymbol{\sigma} + \mathbf{b}_v = \mathbf{0} \text{ in } \Omega, \quad (36a)$$

$$\boldsymbol{\sigma}^T \mathbf{v} - \mathbf{t} = \mathbf{0} \text{ in } \Gamma_d. \quad (36b)$$

Equations (36a)-(36b) represent the internal equilibrium and natural boundary conditions of the body, complemented by the following equilibrium conditions across the discontinuity:

$$\begin{aligned} \mathbf{t} &= -(\boldsymbol{\sigma}^+)^T \mathbf{n}^+ \\ \mathbf{t} &= (\boldsymbol{\sigma}^-)^T \mathbf{n}^- \end{aligned} \quad \text{on } \Gamma_d \quad (37)$$

and the kinematic condition

$$\mathbf{u} = \bar{\mathbf{u}} \text{ on } \Gamma_u. \quad (38)$$

Equation (38) states the essential boundary conditions of the variational problem.

5.2. Numerical Formulation. Once the functional of the discrete approach of the embedded discontinuity formulation is defined, the discretization of the domain by the finite

element method is carried out by means of the displacement and strain kinematic, developed in Section 3. This is given as

$$\mathbf{u} = \mathbf{N} \hat{\mathbf{u}} + \mathbf{N}_c \tilde{\mathbf{u}}, \quad (39)$$

$$\boldsymbol{\varepsilon} = \nabla^s \mathbf{u} = \mathbf{B} \hat{\mathbf{u}} + \mathbf{B}_c \tilde{\mathbf{u}}, \quad (40)$$

where $\hat{\mathbf{u}}$ and $\tilde{\mathbf{u}}$ are the regular and not regular displacements, respectively. The matrix \mathbf{N} contains the standard shape functions. Shape functions associated with nodes belonging to Ω^+ are contained in matrix \mathbf{N}_c .

As for standard finite element method, matrices \mathbf{B} and \mathbf{B}_c , given in equation (40), contain derivatives of the corresponding shape functions in matrices \mathbf{N} and \mathbf{N}_c .

Substitution of equations (39) and (40) into the energy functional defined in equation (33), and its corresponding minimization, leads to the algebraic system of equation,

$$\begin{bmatrix} \mathbf{K}_{\hat{\mathbf{u}}\hat{\mathbf{u}}} & \mathbf{K}_{\hat{\mathbf{u}}\tilde{\mathbf{u}}} \\ \mathbf{K}_{\tilde{\mathbf{u}}\hat{\mathbf{u}}}^T & \mathbf{K}_{\tilde{\mathbf{u}}\tilde{\mathbf{u}}} \end{bmatrix} \begin{bmatrix} \hat{\mathbf{u}} \\ \tilde{\mathbf{u}} \end{bmatrix} = \begin{bmatrix} \mathbf{f}_{\text{ext}} \\ 0 \end{bmatrix}, \quad (41)$$

with

$$\mathbf{K}_{\hat{\mathbf{u}}\hat{\mathbf{u}}} = \int_{\Omega} \mathbf{B}^T \mathbf{C} \mathbf{B} d\Omega, \quad (42)$$

$$\mathbf{K}_{\tilde{\mathbf{u}}\tilde{\mathbf{u}}} = \int_{\Omega} \mathbf{B}_c^T \mathbf{C} \mathbf{B}_c d\Omega, \quad (43)$$

$$\mathbf{K}_{\tilde{\mathbf{u}}\hat{\mathbf{u}}} = \int_{\Omega} \mathbf{B}_c^T \mathbf{C} \mathbf{B} d\Omega + \int_{\Gamma_d} \mathbf{N}_c^T \mathbf{T} \mathbf{N}_c d\Gamma, \quad (44)$$

and external forces vector

$$\mathbf{f}_{\text{ext}} = \int_{\Omega} \mathbf{N}^T \mathbf{b}_v d\Omega + \int_{\Gamma_t} \mathbf{N}^T \bar{\mathbf{t}} d\Gamma. \quad (45)$$

Here, the coefficient matrix is symmetric and unlike other discontinuity formulations [26–28, 33], there are nonzeros along its leading diagonal. The inelastic response is related to the term $\int_{\Gamma_t} \mathbf{N}^T \bar{\mathbf{t}} d\Gamma$ of the submatrix $\mathbf{K}_{\tilde{\mathbf{u}}\tilde{\mathbf{u}}}$.

6. Tractions Equilibrium

The interpolation of the displacement jump field by the finite element method of the (KOS) formulation considers the shape function \mathbf{N}_c . This kind of interpolation is a proper way to consider that the localization band width b_d is different from zero; but, when this band collapses into a line, i.e., discrete discontinuity, the matrix \mathbf{N}_c has the meaning of the identity matrix which leads to consider tractions at the discontinuity surface in the local framework.

The case, when $b_d = 0$, may lead to a nonproper enforcement of tractions continuity which only satisfies equilibrium for cases depending in the geometry of the element. To show this, consider the element of Figure 9.

The discontinuity crossing the element is parallel to side 1–2 with length l_{12} ; \mathbf{n} is the normal to the discontinuity, and h is the height of the triangle. The angle β is measured from the x axis to the side 1–2, and α is the angle between the x axis and the normal to the referred side.

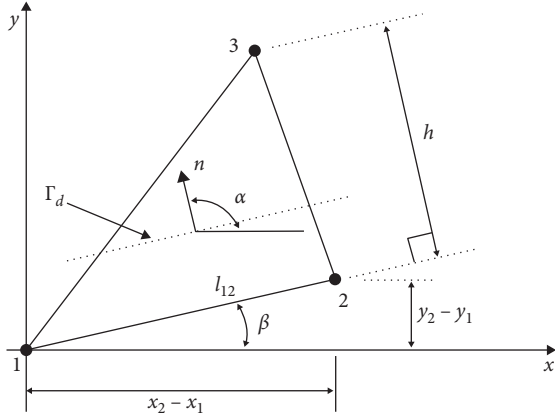


FIGURE 9: Projection of the discontinuity to the opposite side to node 3.

The area of the element is $A = l_{12}h/2$; hence, $2A = l_{12}h$, and from the geometry of the element and the angle β , the following relations are derived:

$$\begin{aligned}\cos \beta &= \frac{x_2 - x_1}{l_{12}}, \\ \sin \beta &= \frac{y_2 - y_1}{l_{12}}.\end{aligned}\quad (46)$$

Furthermore, for the element shown in Figure 9, the matrix \mathbf{B}_c is defined as

$$\mathbf{B}_c = -\frac{1}{2A} \begin{bmatrix} y_1 - y_2 & 0 \\ 0 & x_2 - x_1 \\ x_2 - x_1 & y_1 - y_2 \end{bmatrix}. \quad (47)$$

Rewritten equation (47) by means of relationships derived from the geometry of the element and using the angle α instead of β ,

$$\mathbf{B}_c = \frac{1}{h} \begin{bmatrix} \cos \alpha & 0 \\ 0 & \sin \alpha \\ \sin \alpha & \cos \alpha \end{bmatrix}. \quad (48)$$

It may be observed from equation (48) that it is like the normal-projection matrix, which contains the components of vector \mathbf{n} , normal vector to the surface Γ_d ; this is given as

$$\mathbf{P}_n = \begin{bmatrix} \cos \alpha & 0 \\ 0 & \sin \alpha \\ \sin \alpha & \cos \alpha \end{bmatrix}. \quad (49)$$

The difference between matrices (48) and (49) is the term $1/h$ which makes that traction continuity cannot be imposed correctly. Once a discontinuity appears in the element, the equilibrium on Γ_d is given as

$$\int_{\Omega} \mathbf{B}_c^T \left(\hat{\boldsymbol{\sigma}}^u + \frac{\tilde{\boldsymbol{\sigma}}^u}{\approx 0} \right) d\Omega + \int_{\Gamma_d} \mathbf{t} d\Gamma = 0. \quad (50)$$

Hence, the equilibrium only depends of regular stresses $\hat{\boldsymbol{\sigma}}^u$, derived from the regular displacements part $\hat{\mathbf{u}}$, and tractions \mathbf{t} developed on the discontinuity surface.

After some algebraic operations, it may be shown that tractions are expressed as follows:

$$t_n = \frac{1}{2l_d} [y_1 - y_2] \sigma_x, \quad (51a)$$

$$t_s = \frac{1}{2l_d} [x_2 - x_1] \sigma_y. \quad (51b)$$

These results show that traction continuity is not satisfied since the correct tractions are $t_n = \sigma_x$ and $t_s = \sigma_y$. According to this, it is derived that equilibrium is satisfied only when

$$2l_d = (y_1 - y_2), \quad (52a)$$

$$2l_d = (x_2 - x_1). \quad (52b)$$

6.1. Correct Definition of the Discontinuity Length. In what follows, a consistent way for a correct enforcement of equilibrium on the discontinuity surface is given by means of geometrical relationships. The formulation is developed for a constant strain triangle with the discrete approach of the symmetric embedded discontinuity model.

The first part of equation (41) gives equilibrium in the element nodes, i.e., global equilibrium, whereas the second states traction equilibrium at the discontinuity surface, elemental equilibrium, as

$$\int_{\Omega} \mathbf{R}^T \mathbf{B}_c^T \left(\hat{\boldsymbol{\sigma}}^u + \tilde{\boldsymbol{\sigma}}^u \right) d\Omega + \int_{\Gamma_d} \mathbf{t} d\Gamma = 0, \quad (53)$$

where \mathbf{R} is the rotation matrix, from local coordinates to global coordinates, defined as

$$\mathbf{R} = \begin{bmatrix} \cos \theta & -\sin \theta \\ \sin \theta & \cos \theta \end{bmatrix}. \quad (54)$$

From equation (53), it is observed that equilibrium depends of tractions \mathbf{t} , defined on the surface Γ_d , and internal forces of the solitary node i (Figure 10).

According to the construction of the matrix \mathbf{B}_c , which is derived from the element geometry, the correct imposition of equilibrium on the discontinuity occurs only over a specific surface, depending on the discontinuity geometry. This is a drawback of the presented formulation which makes it dependent of the geometry of the element, unlike the nonsymmetric embedded discontinuity formulation (see [22, 29, 33, 39]) in which the equilibrium is invariant with respect to the geometry. From this condition, the localization of the discontinuity is a variable in the problem for the present KOS formulation [4, 5] (see Figure 10). To show this condition, consider the initial state for $\sigma_I > \sigma_{t0}$,

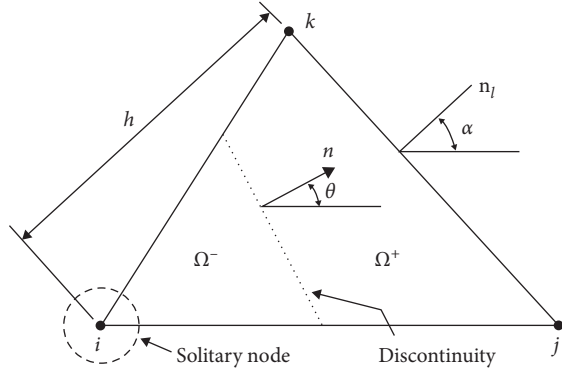


FIGURE 10: Geometry parameters for constructions of the matrix \mathbf{B}_c .

$$\begin{aligned} t_n &= \sigma_{t0} = \sigma_I, \\ t_s &= 0, \\ \llbracket \mathbf{u} \rrbracket &\approx 0. \end{aligned} \quad (55)$$

The state defined in equation (55) leads to the following form of equation (53):

$$\begin{aligned} t_n l_d &= \frac{A}{h} \left[\cos \theta (\cos \alpha \sigma_x + \sin \alpha \sigma_{xy}) \right. \\ &\quad \left. + \sin \theta (\sin \alpha \sigma_y + \cos \alpha \sigma_{xy}) \right]. \end{aligned} \quad (56)$$

This last equation is rewritten by means of trigonometric functions and the next shear stress relation,

$$\sigma_{xy} = \frac{1}{2} \tan 2\theta (\sigma_x - \sigma_y), \quad (57)$$

to obtain, after some algebra,

$$\begin{aligned} t_n \frac{l_d h}{A} \frac{1}{\cos(\theta - \alpha)} &= \frac{1}{2} \left[\frac{(\sigma_x - \sigma_y)}{\cos(\theta - \alpha)} (\cos(\theta + \alpha)) \right. \\ &\quad \left. + \tan 2\theta \sin(\theta + \alpha) + (\sigma_x + \sigma_y) \right]. \end{aligned} \quad (58)$$

The initial condition $t_n = \sigma_I$ implies that the right-hand side of equation (58) must be equal to σ_I . This is satisfied if and only if the first term is equal to

$$\cos(\theta + \alpha) + \tan 2\theta \sin(\theta + \alpha) = \sqrt{1 + \tan^2 2\theta \cos(\theta - \alpha)}. \quad (59)$$

To prove this, both sides of equation (58) are squared to obtain, after some algebra work and considering trigonometric identities,

$$\sin 2\theta \sin 2\alpha = \sin 2\theta \sin 2\alpha, \quad (60)$$

proving equality of equation (59).

Once equation (59) has been proved, the right-side of equation (58) is replaced by the principal stress σ_I and $t_n = \sigma_I$ to obtain

$$l_d = \frac{A}{h} \cos(\theta - \alpha). \quad (61)$$

Equation (61) defines the surface discontinuity geometry which guarantees the equilibrium of tractions defined by equation (53).

It may exhibit another way to enforce tractions equilibrium across the discontinuity surface, by projecting stresses to a surface parallel to the opposite side of the solitary node i (Figure 10), obtaining the next discontinuity geometry definition:

$$l_d = \frac{A}{h}. \quad (62)$$

Enforcement of tractions equilibrium on the surface defined by equation (62) makes the KOS formulation strongly dependent on the mesh configuration since the discontinuity must be parallel to one side of the element.

7. Numerical Simulation

Two numerical examples are presented to show the numerical and theoretical consistency of the KOS formulation. In both examples, damage is simulated by considering only the mode-I of failure for quasi-brittle materials. The discontinuity is introduced perpendicular to the direction of the maximum principal stress.

7.1. Uniaxial Tension Test. In this example, the mechanical response of a specimen subjected only to a tension state is analysed. This problem was studied, with numerical and experimental models, by Van Vliet [40], to get insight into the physical mechanism underlying the size effect in quasi-brittle materials, such as concrete and rock.

The geometry is shown in Figure 11. Its characteristic dimension D is taken equal to 200 mm, radius $r = 145$ mm, depth equal to 100 mm, and eccentricity $e = D/50$ mm.

The assumed material properties were the average of those reported for the specimen type "05C04N30"; this is given as follows: elastic modulus $E = 39.8$ GPa, Poisson ration $\nu = 0.20$, tensile strength $\sigma_{t0} = 2.57$ MPa, and fracture energy $G_F = 0.1219$ N/mm.

To guarantee a uniform load transfer along the top and bottom parts of the specimen, two steel plates were introduced in the laboratory experiments, allowing a free rotation. In the numerical model, this condition was reproduced by means of two layers of elements with the material properties of the steel employed in the experimental tests.

In the laboratory experiments, the specimen was fully instrumented with LVDTs (linear variable displacement transducers) to obtain the deformation of its middle cross section. For the present numerical model, only the deformation along the vertical axis is considered. Figure 11 shows the reference points chosen to measure the vertical deformation; initially separated a distance $L_s = 0.6 D$.

A structured finite element mesh, with triangle elements, is shown in Figure 12. Plane stress condition was assumed for the analysis.

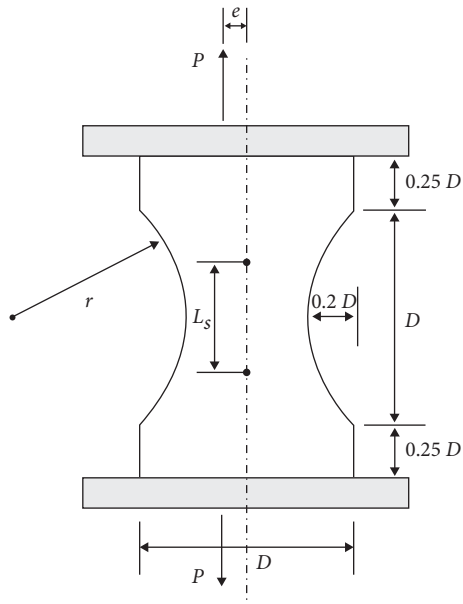


FIGURE 11: Plate subjected to an eccentric load.

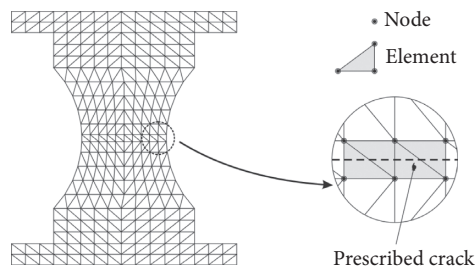


FIGURE 12: Structured mesh with triangle elements.

In this example, the crack pattern was prescribed with the aim of validating the application of the KOS formulation to problems where the propagation of the crack is previously known. However, this does not invalidate its application to problems where the crack pattern is not known at initio.

In Figure 13, the curve deformation versus load is shown. Two numerical responses are plotted for two different softening laws. The continuous thin line corresponds to a linear softening and the continuous thick line is for an exponential softening. Experimental results, reported by Van Vliet [40], are plotted with a dotted line. It is observed that the ascendant branch is correctly reproduced by the present numerical simulation. There exists a small difference between the experimental peak load and the obtained with this study.

This fact is due to the damage model used, which considers that mode-II occurs together with mode-I in brittle form, without energy dissipation [4, 5, 18].

Regarding the rigid body motion, assumed in the present formulation of the two parts in which the solid is divided, this kinematics is observed in Figure 14.

The deformed mesh is shown in Figure 14(a), in which it may be appreciated that element located in the middle height

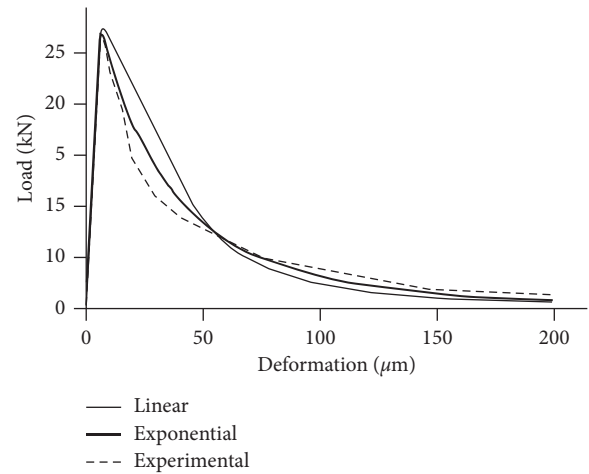


FIGURE 13: Deformation versus load.

is completely crossed by the discontinuity, whereas the rest of elements, outside of this zone, do not undergone any damage. Similarly, in Figure 14(b), maximum principal stresses σ_I are plotted.

The proposed embedded discontinuity formulation, in its KOS approximation, guarantees rigid body motion of the two parts in which the solid is divided by the crack.

It is important to point out that, as expected from the numerical formulation and analysing equation (43), the energy dissipation only takes place on elements crossed by the discontinuity, whereas the rest unload elastically without energy dissipation.

7.2. Single-Notched Four-Point Beam. The four-point shear test, simulated by many authors, by means of continuum models [36, 41, 42], the embedded discontinuity formulation [5, 43–45], and meshless methods [46, 47], is addressed in this section.

Since the pioneer experimental work of Arrea and Ingraffea [47], this type of experimental geometry has been used to study the damage process under mixed mode failure (see Schlangen [48, 49]).

For quasi-brittle materials, like concrete, the fracture is locally driven by the maximum tensile stress [41]. This four-point shear problem undergoes a tension-compression state which gives rise to a curved propagation of the discontinuity, starting from the notch tip and following an inclined direction.

Figure 15 illustrates the loading system applied to the beam, which is asymmetric, and leads to a cracking failure dominated by mode-I. The material properties as well as the geometry of the problem were taken from the work of Schlangen [49].

The geometry is shown in Figure 15 with its dimensions given in millimetres; the depth is 100 mm. At the top of the beam, and symmetrically with respect to a vertical axis, there is a notch of 5 mm width and 20 mm depth. All relevant dimensions and supports, at top and bottom, of the beam are shown in the same figure.

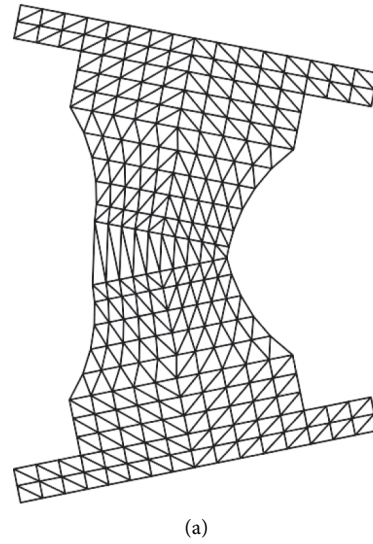


FIGURE 14: Rigid body motion: (a) deformed mesh and (b) principal stresses.

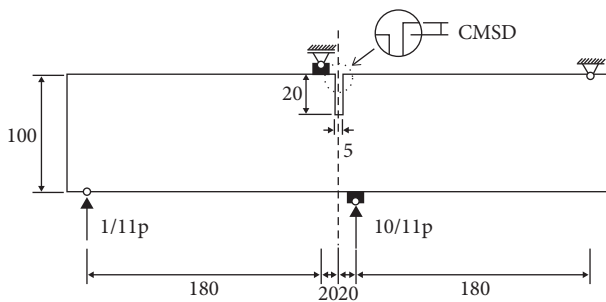


FIGURE 15: Single-notched four-point beam.

With respect to the material properties, these were taken for one series of the laboratory experiments [49], for beam type SEN. The material data are elastic modulus $E = 30$ GPa, Poisson ratio $\nu = 0.20$, and fracture energy $G_F = 0.10$ N/mm. Two tensile strengths were considered, $\sigma_{t0} = 2.8$ MPa and $\sigma_{t0} = 3.0$ MPa.

To compare experimental and numerical results, for the present simulation, the sliding displacement of the crack mouth (CMSD) was measured. This CMSD is the relative vertical displacement between both sides of the notch (see Figure 15).

As it may be seen from Figure 15, the supports are applied in the top of the beam. The left one has restricted just the vertical displacement, whereas that located at the right restricts vertical and horizontal displacements.

The mesh used for the discretization of the domain consists of triangle elements. Unlike the uniaxial tension test example, for this case, the mesh is nonstructures as it is observed in Figure 16.

In zones where loads are applied, additional elements were considered to avoid a stress concentration and obtain a smooth distribution.

The analysis was carried out considering a plane stress state, and a discontinuity is introduced when the principal

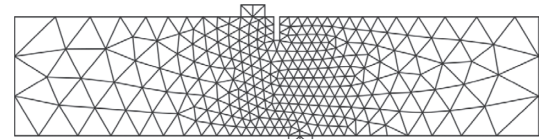


FIGURE 16: Nonstructured mesh for the beam geometry.

stress σ_I reaches the tensile stress of the material, according to the Rankine criterion. The effect of mode-II effect was neglected.

Unlike the uniaxial tension example, where crack pattern was prescribed, in this problem the crack propagation is not a priori enforced, and its path is determined by the direction of the maximum principal stress. The crack is introduced perpendicular to the σ_I direction. This characteristic of introducing the crack without knowing its trajectory makes the embedded discontinuity formulation very promising in problems where the crack propagation across a continuum body is needed. Furthermore, the remeshing process associated with crack propagation, when standard finite elements are used, is eliminated.

The numerical response, load versus CMSD, is shown in Figure 17. The curve corresponding to the experimental test is plotted in continuous thick line. Numerical results, using an exponential softening law, are plotted for a tensile strength of $\sigma_{t0} = 2.8$ MPa with continuous thin line, and the dotted line corresponds to $\sigma_{t0} = 3.0$ MPa.

In this figure, it is possible to appreciate that numerical results derived from the presented formulation reproduce with a great accuracy the ascendant branch of the experimental curve.

Regarding the experimental results, it is observed that the numerical response coincides only until about $P = 10$ kN, likely when the ascendant branch ends, and from this point the response is different. This situation may be attributed in lower grade to the used material properties in the numerical simulation and second to the important

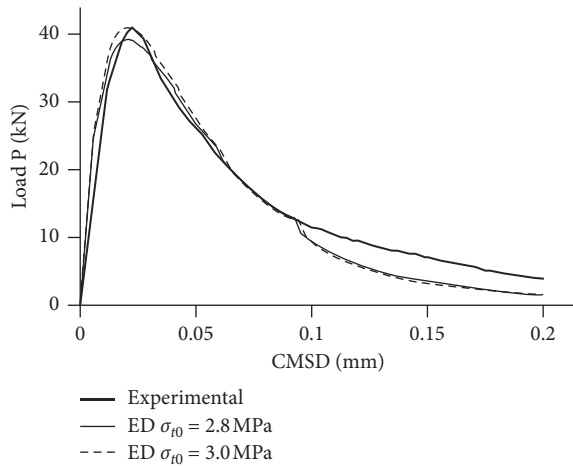


FIGURE 17: Load versus CMSD for the four-point beam.

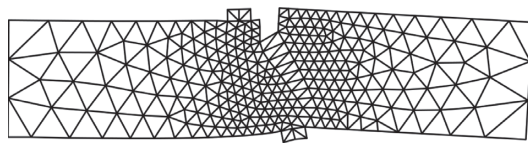


FIGURE 18: Deformed mesh for the four-point beam.

influence of the modelling of the supports used in the experiments. In the simulation, different support systems were considered. In each case, the response was strongly influenced by the support system.

Regarding the unloading branch, it is observed that the numerical and experimental curves are almost equal until a CMSD of 0.1 mm where there is a rapid descend in the numerical response attributable to the lack in the computed crack propagation, maximum principal stress criterion, when an isotropic damage model is used. This problem arises when the crack reaches the last elements located in the bottom part of the beam, leading to a hydrostatic stress state. Despite this, it is important to point out that the numerical simulation reproduces with a good accuracy the global response of the solid, especially the ductile behaviour of the material.

In Figure 18, the deformed mesh is shown. In this figure, it may be observed that the crack pattern is curved where the inelastic response is located, while the bulk unloads elastically. A zoom to the centre of the beam where the crack propagates is shown in Figure 19. The crack pattern which is not a priori enforced is plotted with continuous thick line. Since all the intraelement cracks are forced to pass through the centroid of the elements, the experimental crack pattern cannot be accurately reproduced. To improve this, it is necessary to enforce the crack path continuity across the elements together with a finer mesh.

Finally, in Figure 20, the maximum principal stresses σ_I are plotted. In this figure, it is observed that the maximum values of the stresses occur in elements located in the crack pattern while those in the bulk undergo a linear elastic unloading process, giving a rigid body motion of the two parts in which the continuum is divided by the macrocrack.

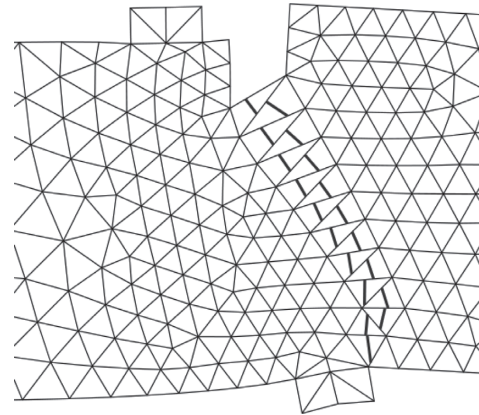


FIGURE 19: Crack pattern across elements.

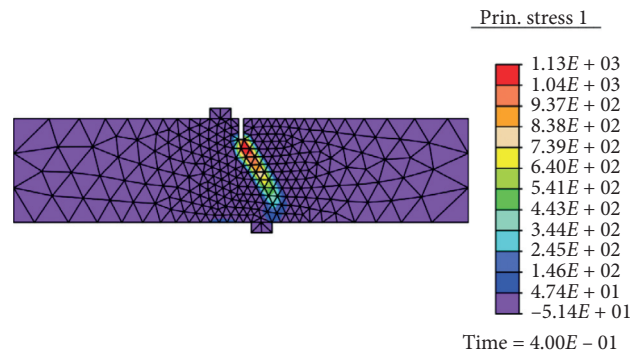


FIGURE 20: Principal stress σ_I , with elastic unloading of the bulk.

8. Conclusions

In this paper, the kinematical optimal symmetric approach of the embedded discontinuity formulation is presented. Its variational and numerical formulations are developed in a consistent way within the finite element method framework. From this, it is shown that the field equation of the boundary value problem is derived in a natural way, and the equilibrium at the discontinuity surface is satisfied. However, when the FEM is used to approximate the solution, traction equilibrium depends on the discontinuity geometry. To guarantee the equilibrium in the numerical model, it is shown that the discontinuity length is a variable to consider in the formulation; otherwise, the equilibrium is not satisfied.

The validity of the presented formulation is evaluated by means of two numerical examples. The first one is a simple tension test and the other is the classical four-point beam with a single notched at its upper face. In both examples, a model-I of failure was considered.

In general, it is shown that the symmetric embedded discontinuity formulation can give robust results when the traction equilibrium across the discontinuity is evaluated in a specific surface, according to the new introduced length variable. In order to improve the numerical results, constitutive models, which consider a mixed mode of failure

I-II, could be considered in the numerical implementation, guaranteeing a consistent energy dissipation.

Data Availability

The experimental data used to support the study have been obtained from reports of other researchers. Specifically, (a) uniaxial tension test problem: M. R. A. V. Vliet, "Size effect in tensile fracture of concrete and rock," Ph.D. Thesis, Delft University of Technology, Delft, the Netherlands, 2000, and (b) single-notched four-point beam: E. Schlangen, "Experimental and numerical analysis of fracture process in concrete," Ph. D. Thesis, Eindhoven, the Netherlands, 1993, and data are cited at relevant places as references.

Conflicts of Interest

The authors declare that they have no conflicts of interest.

Acknowledgments

This research was developed with the support of the "Dirección de Asuntos del Personal Académico (DGAPA)" of the National Autonomous University of Mexico through the PAPIIT projects IN116419 and IN106917.

References

- [1] Z. P. Bazant and J. Planas, *Fracture and Size Effect in Concrete and Other Quasibrittle Materials*, CRC Press, Cleveland, OH, USA, 1997.
- [2] J. Lemaitre, *A Course on Damage Mechanics*, Springer-Verlag, Berlin, Germany, 1996.
- [3] G. Z. Voyiadjis and P. I. Kattan, *Damage Mechanics*, CRC Press, Cleveland, OH, USA, 2005.
- [4] J. Retama and G. Ayala, "Modelado del daño en sólidos mediante formulaciones variacionales de discontinuidades interiores," *Revista Internacional de Métodos Numéricos para Cálculo y Diseño en Ingeniería*, vol. 26, pp. 171–177, 2010.
- [5] J. Retama, *Formulation and approximation to problems in solids by embedded discontinuity models*, Ph.D. Thesis, National Autonomous University of Mexico, Mexico City, Mexico, 2010.
- [6] A. Hillerborg, M. Modéer, and P. E. Petersson, "Analysis of crack formation and crack growth in concrete by means of fracture mechanics and finite elements," *Cement and Concrete Research*, vol. 6, no. 6, pp. 773–781, 1976.
- [7] S. H. Song, *Fracture of asphalt concrete: a cohesive zone modeling approach considering viscoelastic effects*, Ph.D. Thesis, University of Illinois, Champaign, IL, USA, 2006.
- [8] M. G. A. Tijssens, *On the cohesive surface methodology for fracture of brittle heterogeneous solids*, Ph.D. Thesis, Eindhoven University of Technology, Eindhoven, Netherlands, 2000.
- [9] Y.-N. Li and Z. P. Bazant, "Eigenvalue analysis of size effect for cohesive crack model," *International Journal of Fracture*, vol. 66, no. 3, pp. 213–226, 1994.
- [10] T. L. Anderson, *Fracture Mechanics*, CRC Press, Cleveland, OH, USA, 1995.
- [11] T. Belytschko, J. Fish, and B. E. Engelman, "A finite element with embedded localization zones," *Computer Methods in Applied Mechanics and Engineering*, vol. 70, no. 1, pp. 59–89, 1988.
- [12] E. Devorkin, "Finite elements with displacement interpolated embedded localization lines insensitive to mesh size and distortions," *International Journal for Numerical Methods in Engineering*, vol. 30, pp. 541–564, 1990.
- [13] J. C. Simo, J. Oliver, and F. Armero, "An analysis of strong discontinuities induced by strain-softening in rate-independent inelastic solids," *Computational Mechanics*, vol. 12, no. 5, pp. 277–296, 1993.
- [14] H. R. Lotfi and P. B. Shing, "Embedded representation of fracture in concrete with mixed finite elements," *International Journal for Numerical Methods in Engineering*, vol. 38, no. 8, pp. 1307–1325, 1995.
- [15] R. Larsson and K. Runesson, "Element-embedded localization band based on regularized displacement discontinuity," *Journal of Engineering Mechanics*, vol. 122, no. 5, pp. 402–411, 1996.
- [16] J. Alfaiate, G. N. Wells, and L. J. Sluys, "On the use of embedded discontinuity elements with crack path continuity for mode-I and mixed-mode fracture," *Engineering Fracture Mechanics*, vol. 69, no. 6, pp. 661–686, 2002.
- [17] G. Juárez and G. Ayala, "Variational formulation of the material failure process in solids by embedded discontinuities model," *Numerical Methods for Partial Differential Equations*, vol. 25, no. 1, pp. 26–62, 2009.
- [18] J. Retama and G. A. Ayala, "Influence of crumb-rubber in the mechanical response of modified Portland cement concrete," *Advances in Civil Engineering*, vol. 2017, Article ID 3040818, 9 pages, 2017.
- [19] M. Jirásek, "Comparative study on finite elements with embedded discontinuities," *Computer Methods in Applied Mechanics and Engineering*, vol. 188, no. 1–3, pp. 307–330, 2000.
- [20] J. Mosler, "On the modeling of highly localized deformations induced by material failure: the strong discontinuity approach," *Archives of Computational Methods in Engineering*, vol. 11, no. 4, pp. 389–446, 2004.
- [21] J. C. Simo and M. S. Rifai, "A class of mixed assumed strain methods and the method of incompatible modes," *International Journal for Numerical Methods in Engineering*, vol. 29, no. 8, pp. 1595–1638, 1990.
- [22] J. Oliver, "Modelling strong discontinuities in solid mechanics via strain softening constitutive equations. Part 1: fundamentals," *International Journal for Numerical Methods in Engineering*, vol. 39, no. 21, pp. 3575–3600, 1996.
- [23] J. C. Simo and F. Armero, "Geometrically non-linear enhanced strain mixed methods and the method of incompatible modes," *International Journal for Numerical Methods in Engineering*, vol. 33, no. 7, pp. 1413–1449, 1992.
- [24] J. Alfaiate, A. Simone, and L. J. Sluys, "Non-homogeneous displacement jumps in strong embedded discontinuities," *International Journal of Solids and Structures*, vol. 40, no. 21, pp. 5799–5817, 2003.
- [25] D. D. da Costa, J. Alfaiate, L. J. Sluys, and E. Júlio, "A discrete strong discontinuity approach," *Engineering Fracture Mechanics*, vol. 76, pp. 1176–1201, 2009.
- [26] G. N. Wells and L. J. Sluys, "Three-dimensional embedded discontinuity model for brittle fracture," *International Journal of Solids and Structures*, vol. 38, no. 5, pp. 897–913, 2001.
- [27] J. Oliver, "Modelling strong discontinuities in solid mechanics via strain softening constitutive equations. Part 2: numerical simulation," *International Journal for Numerical Methods in Engineering*, vol. 39, no. 21, pp. 3601–3623, 1996.
- [28] F. Armero and K. Garikipati, "An analysis of strong discontinuities in multiplicative finite strain plasticity and their relation with the numerical simulation of strain localization in

- solids," *International Journal of Solids and Structures*, vol. 33, no. 20–22, pp. 2863–2885, 1996.
- [29] G. N. Wells, *Discontinuous modelling of strain localization and failure*, Ph.D. Thesis, Delft University of Technology, Delft, The Netherlands, 2001.
- [30] K. Bathe, *Finite Element Procedures*, Klaus-Jürgen Bathe, Berlin, Germany, 2016.
- [31] J. N. Reddy, *An Introduction to the Finite Element Method*, McGraw-Hill, New York, NY, USA, 2006.
- [32] O. C. Zienkiewicz, R. L. Taylor, and J. Z. Zhu, *The Finite Element Method. Its Basis and Fundamentals*, Butterworth–Heinemann, Oxford, UK, 2013.
- [33] J. Alfaiate, "Strong discontinuities embedded in finite elements," Technical Report: Relatório ICIST, DTC No. 09/00, Instituto Superior Técnico, Lisboa, Portugal, 2000.
- [34] R. d. Borst, M. A. Gutiérrez, G. N. Wells, J. J. C. Remmers, and H. Askes, "Cohesive-zone models, higher-order continuum theories and reliability methods for computational failure analysis," *International Journal for Numerical Methods in Engineering*, vol. 60, no. 1, pp. 289–315, 2004.
- [35] M. Elices, G. V. Guinea, J. Gómez, and J. Planas, "The cohesive zone model: advantages, limitations and challenges," *Engineering Fracture Mechanics*, vol. 69, no. 2, pp. 137–163, 2002.
- [36] J. G. Rots, *Computational modeling of concrete fracture*, Ph.D. Thesis, Delft University of Technology, Delft, Netherlands, 1988.
- [37] P. Germain, Q. S. Nguyen, and P. Suquet, "Continuum thermodynamics," *Journal of Applied Mechanics*, vol. 50, no. 4b, pp. 1010–1020, 1983.
- [38] J. C. Simo and T. J. R. Hughes, *Computational Inelasticity*, Springer-Verlag, Berlin, Germany, 1998.
- [39] M. Jirásek, "Finite elements with embedded cracks," Technical Report: LSC Internal Report 98/01, École Polytechnique Fédérale de Lausanne, Lausanne, Switzerland, 1998.
- [40] M. R. A. V. Vliet, *Size effect in tensile fracture of concrete and rock*, Ph.D. Thesis, Delft University of Technology, Delft, Netherlands, 2000.
- [41] M. Jirásek and B. Patzák, "Consistent tangent stiffness for nonlocal damage models," *Computers & Structures*, vol. 80, no. 14–15, pp. 1279–1293, 2002.
- [42] J. K. Pamin, *Gradient-dependent plasticity in numerical simulation of localization phenomena*, Ph.D. Thesis, Delft University of Technology, Delft, Netherlands, 1993.
- [43] E. W. V. Chaves, *A three dimensional setting for strong discontinuities modelling in failure mechanics*, Ph.D. Thesis, Universitat Politècnica de Catalunya, Barcelona, Spain, 2003.
- [44] E. Samaniego, *Contributions to the continuum modelling of strong discontinuities in two-dimensional solids*, Ph.D. Thesis, Universitat Politècnica de Catalunya, Barcelona, Spain, 2003.
- [45] J. M. Sancho, J. Planas, D. A. Cendón, E. Reyes, and J. C. Gálvez, "An embedded crack model for finite element analysis of concrete fracture," *Engineering Fracture Mechanics*, vol. 74, pp. 75–86, 2007.
- [46] T. Rabczuk and T. Belytschko, "Adaptivity for structured meshfree particle methods in 2D and 3D," *International Journal for Numerical Methods in Engineering*, vol. 63, no. 11, pp. 1559–1582, 2005.
- [47] M. Arrea and A. Ingraffea, "Mixed mode crack propagation in mortar and concrete," Technical Report: 81-13, Department of Structural Engineering, Cornell University, Ithaca, NY, USA, 1982.
- [48] E. Schlangen, "Experimental and numerical analysis of fracture processes in concrete," *HERON*, vol. 38, no. 2, 1993.
- [49] E. Schlangen, *Experimental and numerical analysis of fracture processes in concrete*, Ph.D. Thesis, Eindhoven University of Technology, Eindhoven, Netherlands, 1993.
- [50] G. Juárez and G. Ayala, "Variational formulation of the material failure process in solids by embedded discontinuities model," *Numerical Methods for Partial Differential Equations*, vol. 25, no. 1, pp. 26–62, 2009.